

Impulsive waves caused by subaerial landslides

B. Ataie-Ashtiani · A. Nik-Khah

Received: 9 February 2008 / Accepted: 8 May 2008 / Published online: 28 May 2008
© Springer Science+Business Media B.V. 2008

Abstract This paper presents the experimental results of impulsive waves caused by subaerial landslides. A wide range of effective parameters are considered and studied by performing 120 laboratory tests. Considered slide masses are both rigid and deformable. The effects of bed slope angle, water depth, slide impact velocity, geometry, shape and deformation on impulse wave characteristics have been inspected. The impulse wave features such as amplitude, period and also energy conversation are studied. The effects of slide Froude number and deformation on energy conversation from slide into wave are also investigated. Based on laboratory measured data an empirical equation for impulse wave amplitude and period have been presented and successfully verified using available data of previous laboratory works.

Keywords Impulsive wave · Subaerial landslide · Wave energy · Deforming slide · Dam reservoir

1 Introduction

Subaerial landslides falling into water body generate impulsive water waves that are usually referred to as a category of tsunami waves [6]. It is important to investigate on characteristics of the impulsive wave in near and far field in coastal and dam reservoir design [3]. Noda [13] physically modeled horizontal and vertical subaerial landslides by solid block and investigated effective parameters in phenomenon. He defined four different patterns for impulsive waves generated by subaerial landslides as non-linear oscillatory, transition, solitary like and dissipative transient bore. Kamphuis and Bowering [11] initiated a laboratory study program to investigation subaerial landslides generated wave and saw that the characteristic of this wave depend mainly on the slide volume and the Froude number of the slide upon impact with the water. They concluded the velocity of wave propagation may

B. Ataie-Ashtiani (✉) · A. Nik-Khah
Department of Civil Engineering, Sharif University of Technology, Tehran, Iran
e-mail: ataie@sharif.edu

be approximated very closely by solitary wave theory. Huber and Hager [10] carried out a three dimensional experiment by considering granular landslide falling into a water tank. In their experiments the generated wave height was not expressed as a function of the impact Froude number (as in Kamphuis and Bowering study) but it was mainly depend on the values of the non-dimensional landslide volume. Moreover, the results showed that the landslide density plays a minor role in the generation mechanism. Walder et al. [15] studied the near field characteristics of impulsive waves caused by solid block in a two dimensional physical model. Their scaling analysis indicated that the quantities controlling near-field wave properties may be chosen as non-dimensional landslide volume per unit width, non-dimensional submerged time of motion and non-dimensional vertical impact speed. In all of above mentioned studies some empirical equations presented for prediction of maximum wave height and in some of them for the period. Fritz et al. [7–9] performed elegant laboratory experiments on the characteristics of impulsive waves caused by subaerial landslides and the experiments were performed with granular material. They presented empirical equations for predicting pattern of wave based on slide properties and also presented empirical equations for predicting energy conversation from slide to water. Panizzo et al. [14] carried out three dimensional experiments and presented empirical equations for the generated waves characteristics. They concluded the maximum generated wave height is influenced predominantly by non-dimensional time of underwater landslide motion and the surface of the landslide front. A dependence on the inclination angle of the landslide movement also observed. Also it was observed that the impulse waves height considerably vary over distances, r , from the impact point. Table 1 provides some of the most important previous laboratory studies that have performed for subaerial landslides. Ataie-Ashtiani and Malek Mohammadi [1,2] provided an extensive review about the available empirical equations for prediction of impulsive wave characteristics caused by subaerial landslides. They have evaluated the accuracy and applicability of the equations for real cases. They performed scaling analysis on the basis of real cases and accessible experimental data of before researches and defined dimensionless variables which govern the wave feature which will be explained in present paper.

Table 1 Specification of previous laboratory investigations on subaerial landslide generated wave

Ref.	Tank dim.			Bed slope (degree)	Slide mass specifications	Model dim.	Wave stage
	L (m)	W (m)	H (m)				
Noda 1970 [13]	Shallow water tank			–	Solid rectangular box	–	G
Kamphuis and Bowering 1972 [11]	45	1	0.23~0.46	45	Steel box	2VD	G
Huber and Hager 1997 [10]	30.33	0.5	0.5	28~60	Granular material	3D	G, P
Walder et al. 2003 [15]	3.0	0.285	1.0	10~20	Hollow rectangular nylon box	2VD	G
Fritz et al. 2004 [9]	11	0.5	1.0	45	Granular material and PLG	2VD	G, P
Panizzo et al. 2005 [14]	11.5	6	0.8	16~36	Solid rectangular box	3D	G, P

2VD, Two-vertical dimensional; 3D, Three dimensional; PLG, Pneumatic Landslide Generator; G, Generation of impulse wave; P, Propagation of impulse wave

The main objective of this work is to study the characteristics of impulsive waves generated by subaerial landslides in a range of parameters that covers some of the limitations in previous works. In overall, 120 laboratory tests performed and effects of bed slope angle, slide deformation and shape on wave feature and energy are inspected. Finally, laboratory-based equations are presented for estimation of impulse wave amplitude and period and the proposed equations would be verified using available data in previous laboratory works.

2 Experimental set-up

Experiments were set-up in a 2.5 m wide, 1.8 m deep and 25 m long wave tank at Sharif University of Technology. The details of the experimental setup are provided in [5, 12] and a brief description is also provided here. Two inclined planes with adjustable slope from 15 to 60 degrees were made for sliding down solid blocks or sliding materials and another one for observation of run-up of slide-generated waves. The sliding surface was smooth and was also lubricated in order to provide a frictionless slope. A schematic of wave tank and the adjustable slopes are shown in Fig. 1. The specifications of solid steel blocks, used as landslides, are presented in Table 2 and their schematics are shown in Fig. 2.

Validyne DP15 differential pressure transducers were used as wave gages in these experiments. They were located in eight points at the central axis of the tank (ST1 to ST8 shown on Fig. 1). All of the specifications of wave gauges are listed in Table 3. Full information

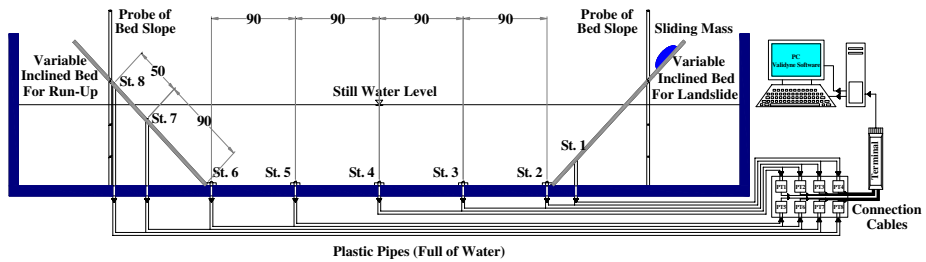


Fig. 1 Schematics of experimental set up for subaerial landslide generated waves, all dimensions are in centimeter

Table 2 Specifications of rigid blocks

No.	Tag no.	V (cm ³)	W _p (g)	W _i (g)	W _w (g)	W _t (g)	A (cm ²)	γ (g/cm ³)
		±1	±0.001	±0.001	±0.001	±0.001	±10	±0.0001
1	B1	3,900	2,370	1,140	3,900	7,410	195	1.9
2	B2	7,800	3,920	3,100	7,800	14,820	390*	1.9
3	B3	1,950	1,570	190	1,950	3,710	98	1.9
4	T1	3,900	2,840	670	3,900	7,410	195	1.9
5	H5	3,100	2,520	270	3,100	5,890	165	1.9
6	H6	5,400	4,050	810	5,400	10,260	165	1.9
7	H7	7,700	5,580	1,350	7,700	14,630	165	1.9

V, Solid block volume; W_p, Weight of perimeter steel plate; W_i, Weight of additional insert plate; W_w, Weight of water; W_t, Total weight of sliding block; γ, Special gravity [= W_t/V]; A, Cross section are *390 for B2a and 600 for B2b (see Fig. 2)

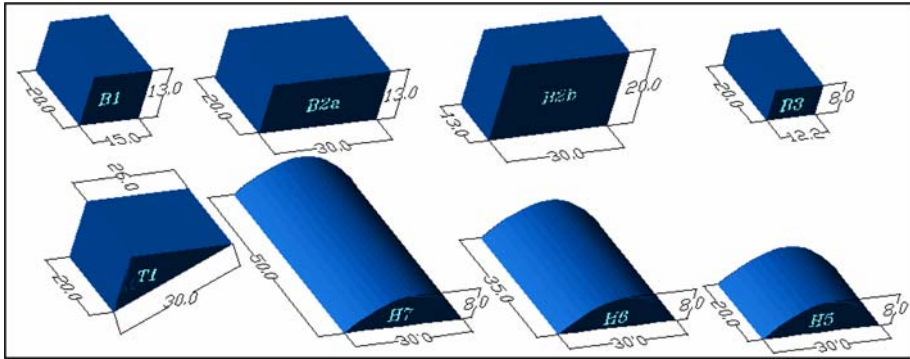


Fig. 2 Schematics of rigid blocks (Dimensions are in Centimeter)

Table 3 Specifications of wave gauges

No.	Gauge station	Sensor technical name	P_{max}	Ac.
1	ST1	DP-15-22-N-1-S-5A	14	± 0.035
2	ST2	DP-15-32-N-1-S-5A	140	± 0.35
3	ST3	DP-15-32-N-1-S-5A	140	± 0.35
4	ST4	DP-15-32-N-1-S-5A	140	± 0.35
5	ST5	DP-15-32-N-1-S-5A	140	± 0.35
6	ST6	DP-15-22-N-1-S-5A	14	± 0.035
7	ST7	DP-15-22-N-1-S-5A	14	± 0.035
8	ST8	DP-15-22-N-1-S-5A	14	± 0.035

P_{max} : Maximum measurable differential pressure (Δp between two sides of diaphragm; cm H_2O)
 Ac.: Accuracy (cm H_2O)

about experimental set-up including tabulated data, pictures and movies are given at http://civil.sharif.ir/~ataie/subaerial_wave/subaerial_landslide_generated_waves.htm.

The main parameters of all of the performed experiments are listed in Table 4. As it can be seen, the variable parameters in performed experiments can be listed as follow: slide specifications such as shape, volume (V_s), thickness (t_s), length parallel to the bed slope (l_s) and rigidity (will be explained), sliding bed slope angle (α), initial position of slide (h_{0C}), and still water depth in wave tank (h_0). The schematic of all parameters is shown in Fig. 3. The numbering procedure of tests is illustrated in Fig. 4. All of the specifications of a case can be observed in its test number.

In deforming-slide tests (cases 103 to 120 in Table 4), granular materials with mean diameter (D_{50}) of 0.7–0.9 cm and $\rho = 1.8–2.0 \text{ g/cm}^3$ is used. The initial shape of granular slide has been set up with triangle section similar to T1 rigid block. This similarity enables us to compare the experimental results in corresponding rigid and deformable-slide tests with the same initial geometry. The deformable-landslide tests are divided into two categories. At the first group of experiments (cases 112 to 120 in Table 4), granular materials are naturally used without any confining fabric, so after releasing of the slide, it has completely deformed and dispersed in the water body. For the second group (cases 103 to 111 in Table 4), granular materials are confined in a very soft fabric. So, the slide continuity is maintained during deformation. These two scenarios are selected to investigate the impulse waves caused by underwater granular deformable slide and interconnected slide such as cohesive deformable slide. Figure 5 shows some sample pictures about three conditions for slide rigidity: rigid, granular material and confined granular material.

Table 4 The experimental program for 120 performed laboratory tests

Case no.	Test no.	Rigidity	Block	h_{0c} (cm)	θ (deg)	h_0 (cm)
1	R-B1-30-11	R	B1	10	30	80
2	R-B1-30-21	R	B1	30	30	80
3	R-B1-30-31	R	B1	50	30	80
4	R-T1-30-11	R	T1	10	30	80
5	R-T1-30-21	R	T1	30	30	80
6	R-T1-30-31	R	T1	50	30	80
7	R-B1-60-11	R	B1	10	60	80
8	R-B1-60-21	R	B1	30	60	80
9	R-B1-60-31	R	B1	50	60	80
10	R-T1-60-11	R	T1	10	60	80
11	R-T1-60-21	R	T1	30	60	80
12	R-T1-60-31	R	T1	50	60	80
13	R-T1-45-11	R	T1	10	45	80
14	R-T1-45-21	R	T1	30	45	80
15	R-T1-45-31	R	T1	50	45	80
16	R-T1-45-12	R	T1	10	45	50
17	R-T1-45-22	R	T1	30	45	50
18	R-T1-45-32	R	T1	50	45	50
19	R-T1-30-12	R	T1	10	30	50
20	R-T1-30-22	R	T1	30	30	50
21	R-T1-30-32	R	T1	50	30	50
22	R-T1-60-12	R	T1	10	60	50
23	R-T1-60-22	R	T1	30	60	50
24	R-T1-60-32	R	T1	50	60	50
25	R-B3-30-11	R	B3	10	30	80
26	R-B3-30-21	R	B3	30	30	80
27	R-B3-30-31	R	B3	50	30	80
28	R-H5-30-11	R	H5	10	30	80
29	R-H5-30-21	R	H5	30	30	80
30	R-H5-30-31	R	H5	50	30	80
31	R-B3-45-11	R	B3	10	45	80
32	R-B3-45-21	R	B3	30	45	80
33	R-B3-45-31	R	B3	50	45	80
34	R-H5-45-11	R	H5	10	45	80
35	R-H5-45-21	R	H5	30	45	80
36	R-H5-45-31	R	H5	50	45	80
37	R-B3-60-11	R	B3	10	60	80
38	R-B3-60-21	R	B3	30	60	80
39	R-B3-60-31	R	B3	50	60	80
40	R-H5-60-11	R	H5	10	60	80
41	R-H5-60-21	R	H5	30	60	80
42	R-H5-60-31	R	H5	50	60	80
43	R-H6-30-11	R	H6	10	30	80
44	R-H6-30-21	R	H6	30	30	80
45	R-H6-30-31	R	H6	50	30	80
46	R-H7-30-11	R	H7	10	30	80
47	R-H7-30-21	R	H7	30	30	80
48	R-H7-30-31	R	H7	50	30	80
49	R-H6-45-11	R	H6	10	45	80
50	R-H6-45-21	R	H6	30	45	80
51	R-H6-45-31	R	H6	50	45	80
52	R-H7-45-11	R	H7	10	45	80
53	R-H7-45-21	R	H7	30	45	80
54	R-H7-45-31	R	H7	50	45	80
55	R-H6-60-11	R	H6	10	60	80

Table 4 continued

Case no.	Test no.	Rigidity	Block	h_{0c} (cm)	θ (deg)	h_0 (cm)
56	R-H6-60-21	R	H6	30	60	80
57	R-H6-60-31	R	H6	50	60	80
58	R-H7-60-11	R	H7	10	60	80
59	R-H7-60-21	R	H7	30	60	80
60	R-H7-60-31	R	H7	50	60	80
61	R-B1-45-11	R	B1	10	45	80
62	R-B1-45-21	R	B1	30	45	80
63	R-B1-45-31	R	B1	50	45	80
64	R-B2a-45-11	R	B2a	10	45	80
65	R-B2a-45-21	R	B2a	30	45	80
66	R-B2a-45-31	R	B2a	50	45	80
67	R-B1-15-12	R	B1	10	15	50
68	R-B1-15-22	R	B1	30	15	50
69	R-B1-15-32	R	B1	50	15	50
70	R-B1-45-12	R	B1	10	45	50
71	R-B1-45-22	R	B1	30	45	50
72	R-B1-45-32	R	B1	50	45	50
73	R-B2a-15-12	R	B2a	10	15	50
74	R-B2a-15-22	R	B2a	30	15	50
75	R-B2a-15-32	R	B2a	50	15	50
76	R-B2a-45-12	R	B2a	10	45	50
77	R-B2a-45-22	R	B2a	30	45	50
78	R-B2a-45-32	R	B2a	50	45	50
79	R-B2a-30-11	R	B2a	10	30	80
80	R-B2a-30-21	R	B2a	30	30	80
81	R-B2a-30-31	R	B2a	50	30	80
82	R-B2b-30-11	R	B2b	10	30	80
83	R-B2b-30-21	R	B2b	30	30	80
84	R-B2b-30-31	R	B2b	50	30	80
85	R-B2a-60-11	R	B2a	10	60	80
86	R-B2a-60-21	R	B2a	30	60	80
87	R-B2a-60-31	R	B2a	50	60	80
88	R-B2b-60-11	R	B2b	10	60	80
89	R-B2b-60-21	R	B2b	30	60	80
90	R-B2b-60-31	R	B2b	50	60	80
91	R-B2a-30-12	R	B2a	10	30	50
92	R-B2a-30-22	R	B2a	30	30	50
93	R-B2a-30-32	R	B2a	50	30	50
94	R-B2b-30-12	R	B2b	10	30	50
95	R-B2b-30-22	R	B2b	30	30	50
96	R-B2b-30-32	R	B2b	50	30	50
97	R-B2a-60-12	R	B2a	10	60	50
98	R-B2a-60-22	R	B2a	30	60	50
99	R-B2a-60-32	R	B2a	50	60	50
100	R-B2b-60-12	R	B2b	10	60	50
101	R-B2b-60-22	R	B2b	30	60	50
102	R-B2b-60-32	R	B2b	50	60	50
103	D-T1-30-11	G.M	T1*	10	30	80
104	D-T1-30-21	G.M	T1*	30	30	80
105	D-T1-30-31	G.M	T1*	50	30	80
106	D-T1-45-11	G.M	T1*	10	45	80
107	D-T1-45-21	G.M	T1*	30	45	80
108	D-T1-45-31	G.M	T1*	50	45	80
109	D-T1-60-11	G.M	T1*	10	60	80
110	D-T1-60-21	G.M	T1*	30	60	80
111	D-T1-60-31	G.M	T1*	50	60	80
112	Dc-T1-30-11	C.G.M	T1*	10	30	80

Table 4 continued

Case no.	Test no.	Rigidity	Block	h_{0c} (cm)	θ (deg)	h_0 (cm)	
R: Rigid block (no deformable slide)	113	Dc-T1-30-21	C.G.M	T1*	30	30	80
G.M.: Granular material (deforming landslide)	114	Dc-T1-30-31	C.G.M	T1*	50	30	80
C.G.M: Confined granular material (confined deforming landslide)	115	Dc-T1-45-11	C.G.M	T1*	10	45	80
	116	Dc-T1-45-21	C.G.M	T1*	30	45	80
	117	Dc-T1-45-31	C.G.M	T1*	50	45	80
	118	Dc-T1-60-11	C.G.M	T1*	10	60	80
	119	Dc-T1-60-21	C.G.M	T1*	30	60	80
	120	Dc-T1-60-31	C.G.M	T1*	50	60	80

*: Initial shape of deforming slides

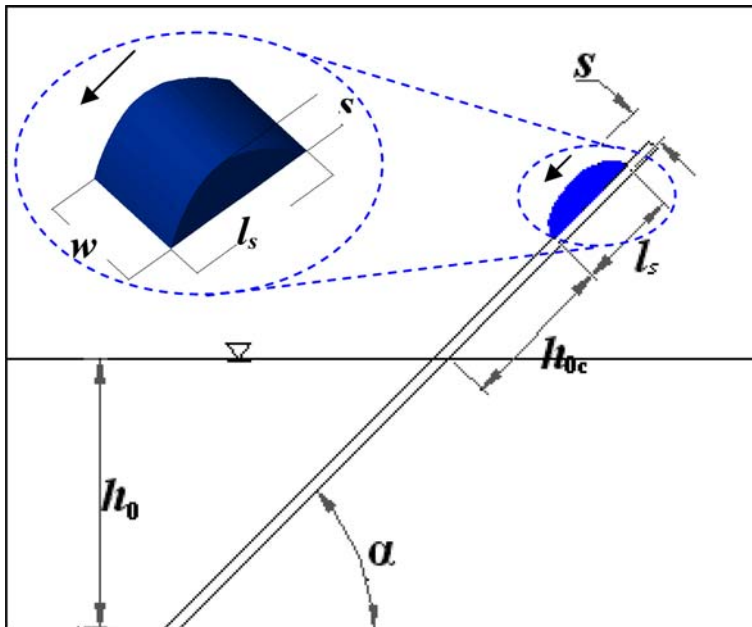


Fig. 3 Definition of geometric parameters for each of tests

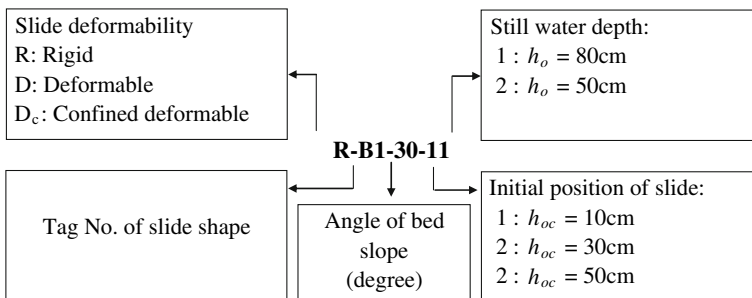


Fig. 4 Numbering procedure of laboratory tests

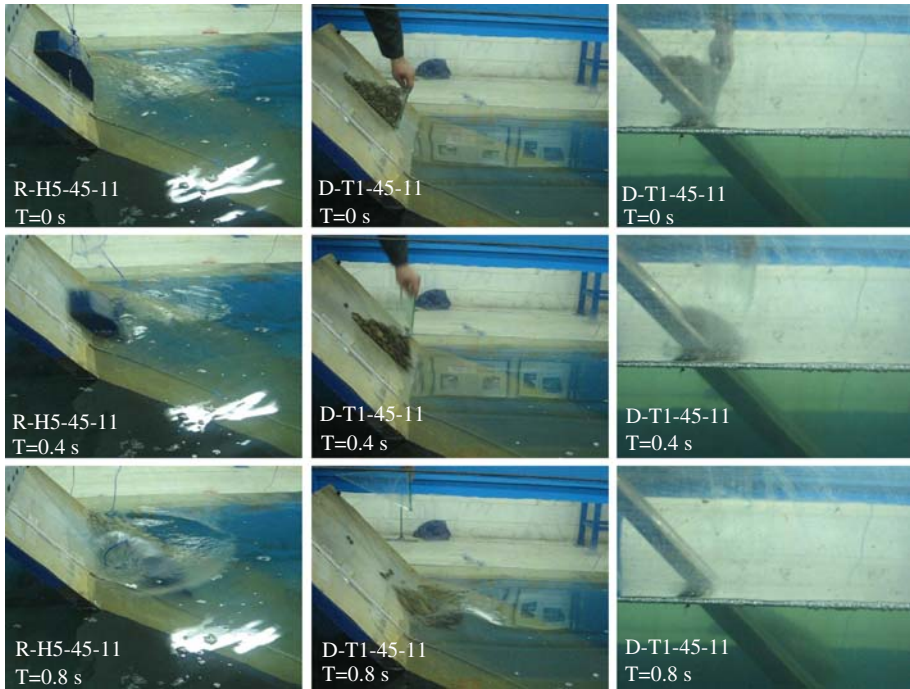


Fig. 5 Three conditions for slide rigidity from left to right: rigid and granular and confined granular material

3 Experimental measurements

The measured data can be categorized as landslide kinematics data and recorded water surface time series at wave gauges. At first category, the location of mass center of slides is determined during sliding down at 0.04-second time step with a 25 frame per second digital camera. Measurement of location done parallel to the bed slope and the $S - t$ time series is determined where S is the slide mass center location. The main parameters of slide kinematics (Slide impact velocity) derived from $S - t$ curve. Second category consists of water surface fluctuations recorded data by gauges located at various distances from slide zone. It leads to recognizing general feature of impulse wave in near and far field and to investigate its energy. Full information about experimental data and related pictures and movies are presented at http://civil.sharif.ir/~ataie/subaerial_wave/subaerial_landslide_generated_waves.htm.

4 Data analysis

4.1 Impact velocity of slide

The slide impact velocity may be determined by Eq. 1 [9]:

$$v_s = \sqrt{2g\Delta z(1 - f \cot \alpha)} \quad (1)$$

where g is gravity; α is the hill slope angle, Dz is the drop height and f is coefficient of friction. Equation 1 developed on the basis of physical formulation of object velocity on the inclined surface (Eq. 2).

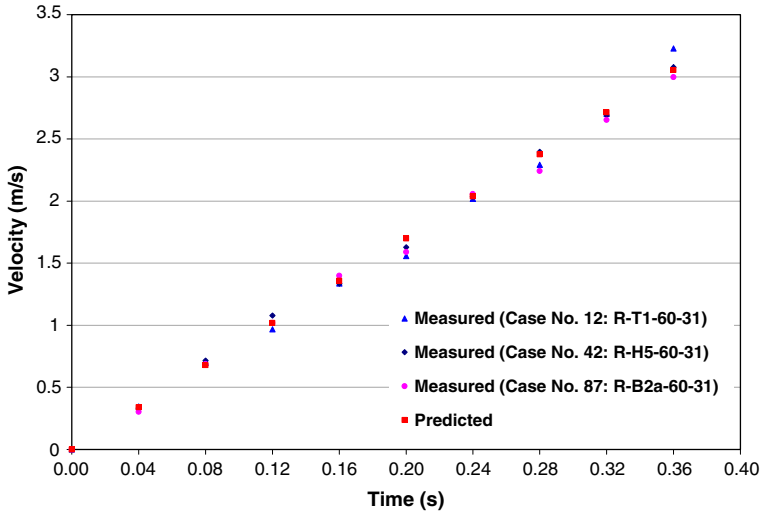


Fig. 6 Comparison between measured values of slide velocity and evaluated slide velocity with Eq. 2

$$v(t) = g(\sin \alpha - f \cos \alpha)t \tag{2}$$

In the present work time series of slide velocity derived from $S - t$ time series (First category of the experimental measurements). Figure 6 presented comparison between measured values of slide velocity and evaluated slide velocity amounts which calculated with Eq. 2. This figure shows that values of slide velocity with this equation are closed to observed slide velocity in laboratory. Then slide impact velocity could be determined by Eq. 1.

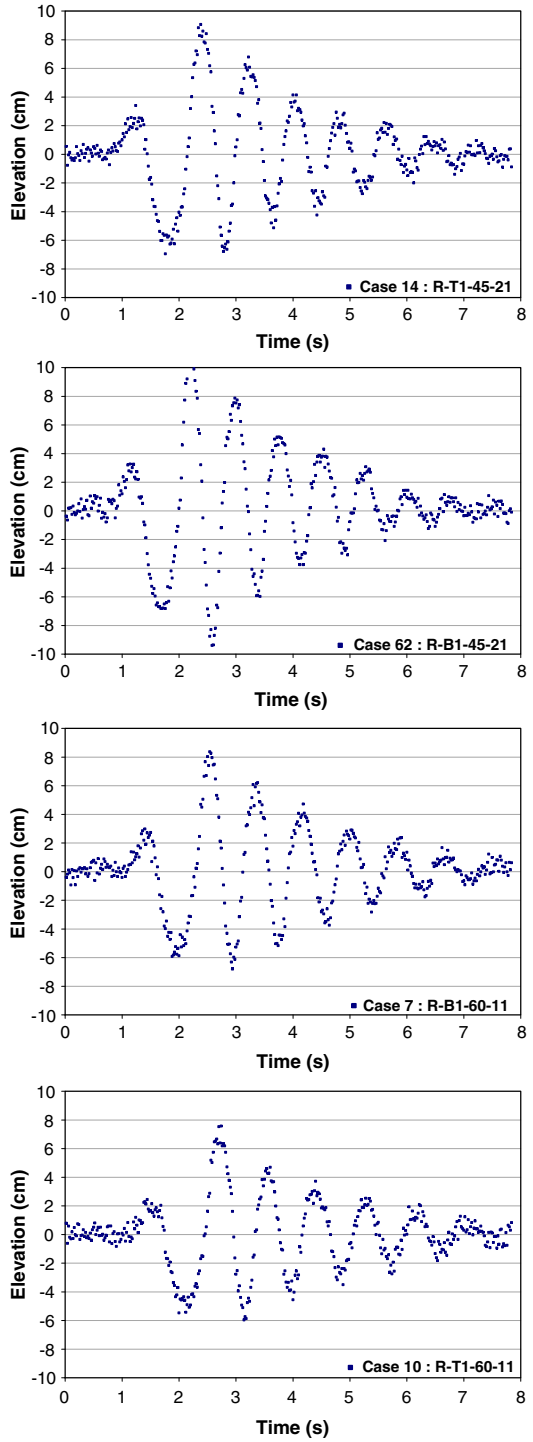
4.2 Impulse wave feature

Figure 7 presents samples of impulsive wave feature observed in laboratory. Wave features presented in this figure have a wave train with a positive amplitude leading wave. Second wave crest has the maximum amplitude in wave train that is followed by smaller oscillatory waves. Results of experiments show that the general patterns of waves in all cases in near and far field are the same but the amplitudes and periods are different. A similar wave pattern can be observed in literature [2,8,10]. This pattern can be predicted by before explained empirical equations presented by Fritze [9].

For investigation on effects of slide deformation on wave feature the recorded data of cases 103 to 120 are analyzed and compared with data of corresponding rigid slide cases. Figure 8 presents a sample of comparison. As seen the patterns of wave features are similar, although wave characteristics vary and deformed landslides reduces maximum amplitude of generated impulse wave ($a_{c \max}$) between 10–17% for confined granular and 25–35% for granular tests comparing to corresponding rigid tests. It also shows an increase of 6–18% for confined granular and 20–30% for granular tests in period of maximum wave (T_{\max}).

In comparison of cases 1 to 12, two blocks B1 and T1 are used which have the same volume, weight and thickness (Table 2). The main difference is the shape of blocks. Figure 9 shows the general feature of impulse waves and as seen the features are not strongly affected by the slide shapes. The amplitude and period are changed less than 10%. Therefore, the effect

Fig. 7 Samples of wave features observed in laboratory



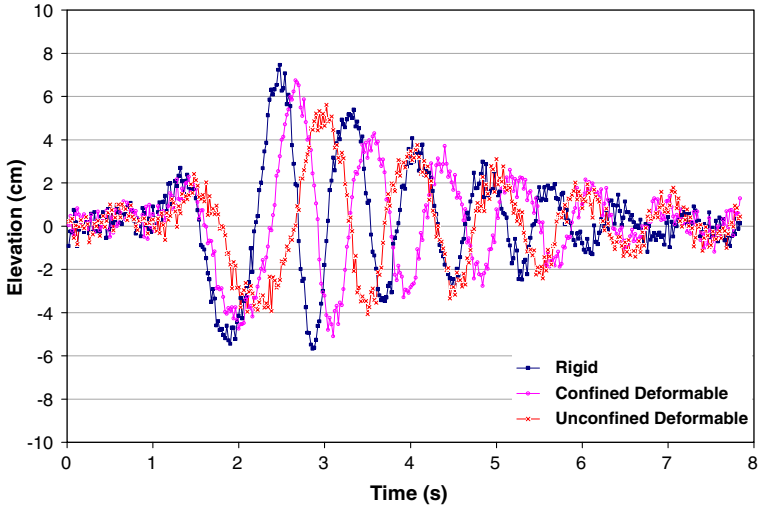


Fig. 8 Slide rigidity effects on impulse wave feature

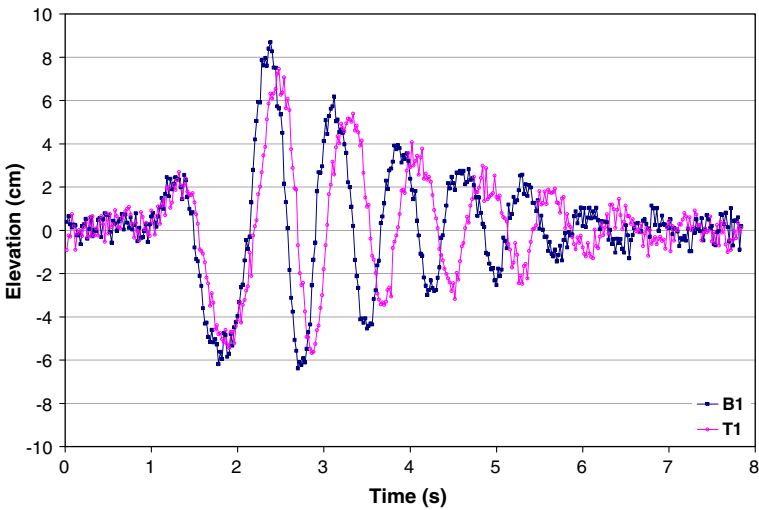


Fig. 9 Slide shape effects on impulse wave feature

of slide shape can be neglected comparing to the main effective parameters explained in the following sections.

Figure 10 shows the time series of wave amplitude at various locations. It can be concluded from this figure that when the impulse wave propagated into the far field, the wave amplitude and steepness decrease, period and wavelength increase. However the general pattern of propagated wave feature is similar to wave pattern of first generated wave features.

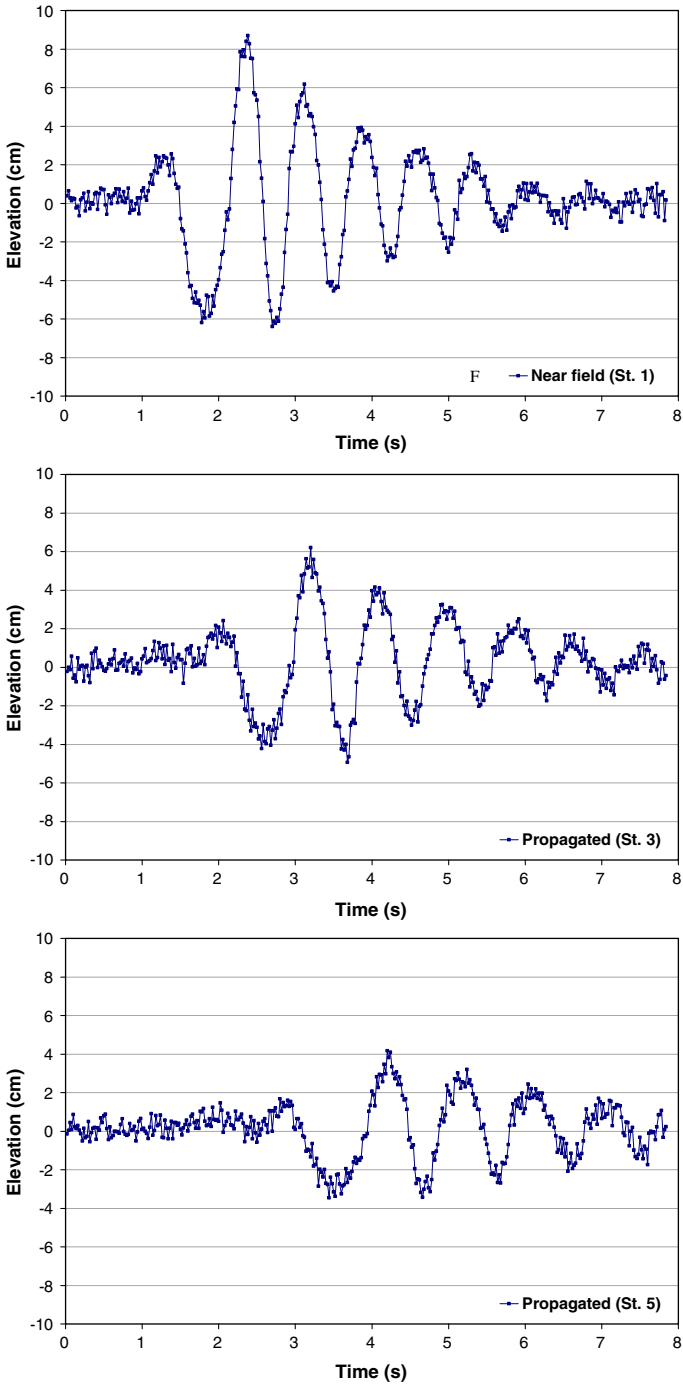


Fig. 10 Time series of wave amplitude at various locations (Case No. 3: R-B1-30-31)

4.3 Impulse wave energy

In this section, the measured data are investigated for impulse wave energy in generation zone. The impulse wave energy is calculated from the recorded time series using the following formula (Eq. 3) [9]:

$$E_w = 2E_{\text{pot}} = \rho_w g c \int \eta^2 dt \tag{3}$$

where E_w is wave energy per unit width (kg.m/s²), E_{pot} is wave potential energy per unit width (kg.m/s²), ρ_w is water density (1,000 kg/m³), g is acceleration due to gravity (9.81 m/s²), c is wave celerity, η is water surface elevation due to still water level and t is time. The landslide energy is also calculated from Watts [16] formula as (Eq. 4):

$$E_s = \rho_s v_s^2 A \tag{4}$$

where E_s is slide energy per unit width (kg.m/s²), ρ_s is slide density (kg/m³), v_s is slide impact velocity (m/s), and A is cross sectional area of blocks (m²). For investigation of energy conversation from sliding block into the wave, the energy conversation ratio is defined similar to Walder et al. [15] as (Eq. 5):

$$e_0 = \frac{E_w(0)}{E_s} \tag{5}$$

where $E_w(0)$ is impulse wave energy at generation zone. Figure 11 shows the variations of energy conversation ratio for different slide Froude numbers (v_s/\sqrt{gh}). This figure shows that increasing of slide Froude number values tend to decreasing of energy conversation ratio. Then it concludes that the greater slide Froude number the less energy conversation ratio. Figure 12 presents effects of slide deformation on energy conversation. It shows for a certain slide Froude number rigid slide and unconfined deformable slide cases had the most and the least energy conversation ratios, respectively. Then it can be concluded that the more rigidity the more energy conversation ratio. Figure 13 presents variation of wave energy at different sensors for three sample experiments. Analyses of data of all experiments show the general pattern of energy propagation is similar in performed experiments using rigid blocks and deformable slide and conclude that slide rigidity and shape have no effect on variation of wave energy under propagation.

4.4 Estimation of impulse wave characteristics

The recorded data at wave gauges are analyzed to present prediction equations for impulse wave characteristics. The main parameters which are considered here are the slide thickness t_s ; the slide length l_s ; the slide width w ; the slide volume V_s ; the slide impact velocity v_s ; the slide underwater travel time t_{0s} ; still water depth h_0 and bed slope angle α on which slide moves; the wave crest amplitude η ; and the wave period T . The main dimensionless variables which govern the wave feature defined by Ataie-Ashtiani and Malek-Mohammadi [4] as: VF^2 , T_s/V and r/h ; Where V is dimensionless slide volume (V_s/wh^2); F_s is slide Froude numbers (v_s/\sqrt{gh}); and T_s is the dimensionless slide underwater travel time ($t_{0s}\sqrt{g/h}$). We define a new dimensionless variable as l_s/t_s to consider the effect of slide shape. The prediction equations are provided for the initial wave amplitude ($a_{c\text{max}}$) and period (T_{max}) are determined as:

$$\frac{a_{c\text{max}}}{h} = \left(0.405 + 0.078 (VF^2)^{1.28}\right) \left(\frac{T_s}{V}\right)^{-0.278} \left(\frac{l_s}{t_s}\right)^{-0.12} \left(\frac{r}{h}\right)^{-0.48} \tag{6}$$

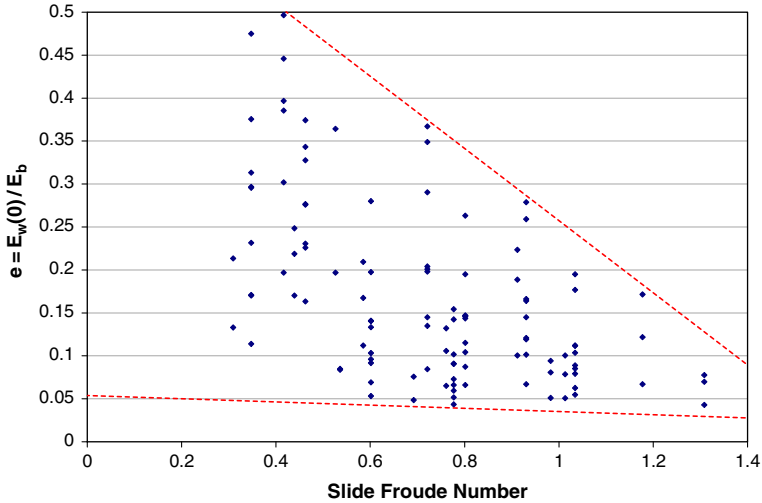


Fig. 11 Variations of energy conversion ratio for different slide Froude numbers (v_s/\sqrt{gh})

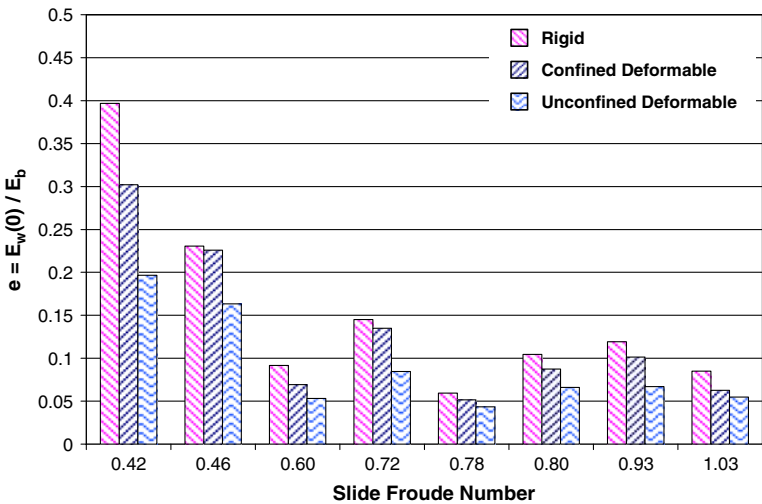


Fig. 12 Effects of deformation on energy conversion

$$\frac{T_{\max}}{\sqrt{g/h}} = \left(4.14 + 3.88 (VF^2)^2\right) \left(\frac{T_s}{V}\right)^{-0.114} \left(\frac{l_s}{t_s}\right)^{0.1} \left(\frac{r}{h}\right)^{0.16} \tag{7}$$

The comparison of predicted wave characteristics and measured data in present work for near field and far field is shown in Figs. 14 and 15, respectively. The verification of prediction equations is made by measured data presented by Kamphuis and Bowering [11], Huber and Hager [5] and Walder et al. [15]. The detail specifications of mentioned previous laboratory works are shown in Table 5. Figure 16 shows the comparison of predicted wave characteristics by Eq. 6 and measured data in that works. As it can be seen, the correlation is generally good and acceptable reliability has been obtained for forecasting Eq. 6. By considering measured

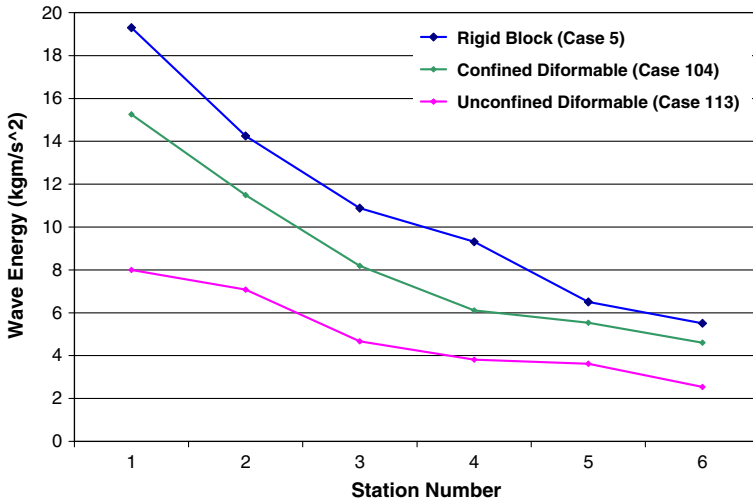


Fig. 13 Wave energy at different sensors

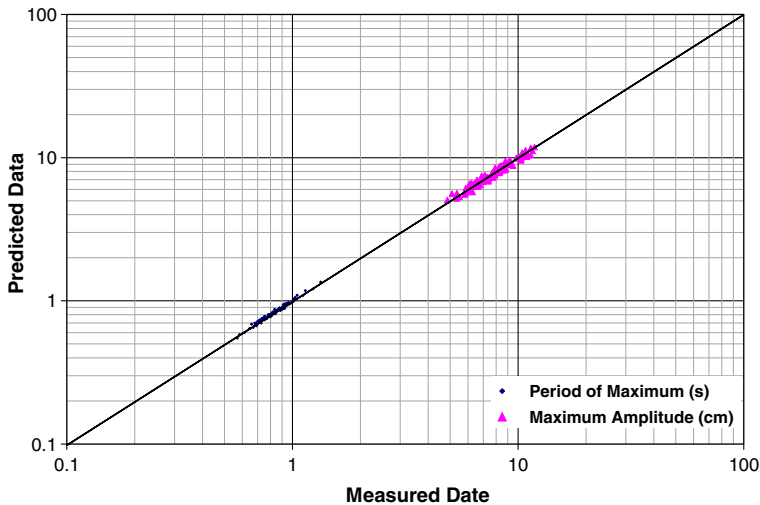


Fig. 14 Verification of presented forecasting equations, near-field wave characteristics

data in present work and in mentioned previous laboratory works all together, the prediction equation for wave amplitude can be provided as (Eq. 8):

$$\frac{a_c \max}{h} = \left(0.398 + 0.076 (VF^2)^{1.27}\right) \left(\frac{T_s}{V}\right)^{-0.26} \left(\frac{l_s}{t_s}\right)^{-0.125} \left(\frac{r}{h}\right)^{-0.48} \quad (8)$$

Figure 17 shows the comparison of predicted wave characteristics by Eq. 8 and measured data for category of experimental data consisting of data presented in present work and mentioned last works. Correlation coefficients of Eqs. 4 and 6 are presented in Table 6 for data of Kamphuis and Bowering [11], Huber and Hager [10] and Walder et al. [15]. In addition averages of these correlation coefficients for Eqs. 6 and 8 are shown in Table 6. Correlation

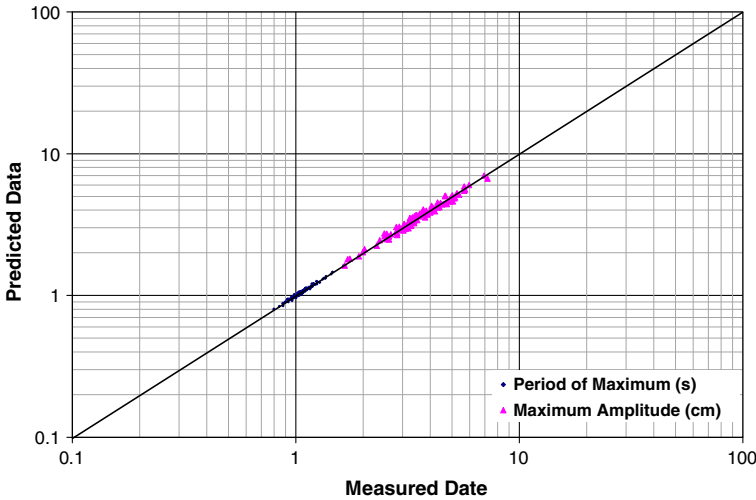


Fig. 15 Verification of presented forecasting equations, far-field wave characteristics

Table 5 Specifications of previous laboratory works

References	Blocks	Water depths (cm)	Slope angles (Deg.)	Range of F_s	Range of VF^2
Kamphuis and Bowering (1970)	One shape	15.2, 22.9, 30.5	19.9, 31.5, 49.3, 69.3	0.281 to 1.051	0.0059 to 0.36
Huber and Hager (1997)	One shape	12, 18, 27, 36	28, 30, 35, 40, 45, 60	0.531 to 3.686	0.001 to 0.51
Walder (2003)	One shape	5.1, 9, 13	11.2, 15, 19.5	1 to 4.1	0.14 to 54.5

coefficients of mentioned equations for data obtained in present work are also presented in this Table. As correlations are generally good and have acceptable reliability it can be concluded the terms used in Eqs. 6 and 8 are useful to investigating subaerial landslide generated wave characteristics.

In real cases of subaerial landslides T_s is a dependent variable and must be calculated. Panizzo [13] developed an empirical equation for estimating T_s .

$$T_s = 0.43V^{-0.27}F^{-0.66}(\sin \alpha)^{1.32} \tag{9}$$

Equation 9 has a good correlation with measured values in our experiments so is used to determine T_s values.

5 Conclusions

Laboratory investigations have been performed on the impulsive waves caused by subaerial landslide. In overall 120 tests have been carried out in laboratory and the data are available on http://civil.sharif.ir/~ataie/subaerial_wave/subaerial_landslide_generated_waves.htm. The data sets can be a very useful resource for theoretical analysis or numerical model validation of other researchers. Both rigid and deforming slide masses were considered. The effects of the main parameters such as bed slope, impact velocity, slide geometry, shape and deformation on the impulse wave characteristics have been inspected.

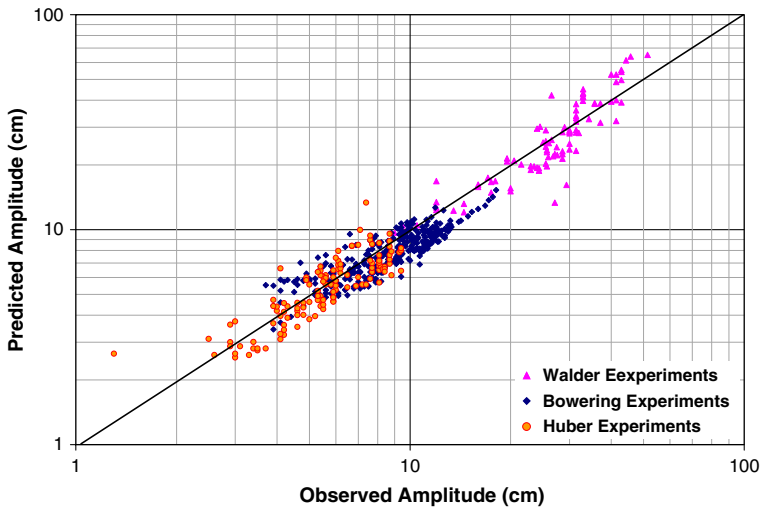


Fig. 16 Verification of Eq. 1 by presented data by Kamphuis and Bowering [11], Huber and Hager [10] and Walder et al. [15]

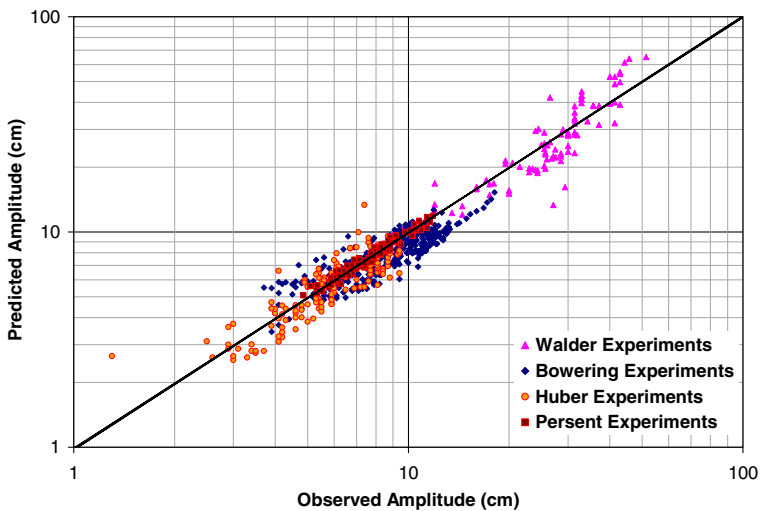


Fig. 17 Verification of Eq. 3 with presented data by Kamphuis and Bowering [11], Huber and Hager [10] and Walder et al. [15] and data obtained in present work

Table 6 Correlation coefficients (r^2)

Formula	r^2 for data presented in literatures			Averaged r^2 for data presented in literatures	r^2 for data obtained in present work
	Kamphuis and Bowering (1970)	Huber and Hager (1997)	Walder (2003)		
(1)	0.87	0.80	0.89	0.85	0.91
(3)	0.88	0.84	0.89	0.87	0.90

Recorded data at near field and far field shows general pattern of generated subaerial impulse wave consists of a wave train with positive leading wave amplitude. Second wave crest of this train has the maximum amplitude that followed by smaller oscillatory waves. Results of experiments show that the general pattern of wave in all cases is the same but the amplitude and period are different.

Laboratory data analysis shows that the maximum wave crest amplitude in subaerial induced waves is strongly affected by bed slope angle, landslide impact velocity, thickness, kinematics and deformation and weakly by landslide shape. Slide deformation makes a maximum reduction on wave crest amplitude down to 35% and a maximum increasing up to 30% on period, although no strong changes in general pattern of subaerial impulse wave features.

Slide shape is not strongly affecting the general feature of impulse wave and at most the amplitude and period are changed less than 10%. The energy conversation from landslide into wave is generally increased where the slide Froude number of landslide decreases. Increasing of slide rigidity makes similar effects.

Finally, forecasting equations are presented for prediction of impulse wave characteristics. These equations have been successfully verified by available laboratory data in previous published works.

References

1. Ataie-Ashtiani B, Malek-Mohammadi S (2007) Near field amplitude of sub-aerial landslide generated waves in dam reservoirs. *Dam Eng* XVII(4):197–222
2. Ataie-Ashtiani B, Malek-Mohammadi S (2008) Mapping impulsive waves due to subaerial landslides into a dam reservoir: case study of Shafa-Roud dam. *Dam Eng* XVIII(3):1–25
3. Ataie-Ashtiani B, Najafi-Jilani A (2006) Prediction of submerged landslide generated waves in dam reservoirs: an applied approach. *Dam Eng* XVII(3):135–155
4. Ataie-Ashtiani B, Najafi-Jilani A (2007) A higher-order Boussinesq-type model with moving bottom boundary: applications to submarine landslide tsunami waves. *Int J Numer Methods Fluids* 53(6):1019–1048
5. Ataie-Ashtiani B, Najafi-Jilani A (2008) Laboratory investigations on impulsive waves caused by underwater landslide. *Coast Eng*. doi:10.1016/j.coastaleng.2008.03.003 (in print)
6. Ataie-Ashtiani B, Shobeyri G (2008) Numerical simulation of landslide impulsive waves by incompressible smoothed particle hydrodynamics. *Int J Numer Methods Fluids* 56(2):209–232
7. Fritz HM, Hager WH, Minor H-E (2003) Landslide generated impulse waves: part 1: instantaneous flow fields. *Exp Fluids* 35:505–519
8. Fritz HM, Hager WH, Minor H-E (2003) Landslide generated impulse waves: part 2: hydrodynamic impact craters. *Exp Fluids* 35:520–532
9. Fritz HM, Hager WH, Minor HE (2004) Near field characteristics of landslide generated impulse waves. *J Waterw Port Coast Ocean Eng* 130(6):287–302
10. Huber A, Hager WH (1997) Forecasting impulse waves in reservoirs. In: Dixneuvième Congress des Grands Barrages C, 31:993–1005. Florence, Italy, Commission International des Grands Barrages, Paris
11. Kamphuis JW, Bowering RJ (1970) Impulse waves generated by landslides. *Proc, 12th Coastal Engineering Conf, ASCE, Reston, Va*, 1:575–588
12. Najafi-Jilani A, Ataie-Ashtiani B (2008) Estimation of near field characteristics of tsunami generation by submarine landslide. *Ocean Eng* 35(5–6):545–557
13. Noda E (1970) Water waves generated by landslides. *J Waterw Port Coast Ocean Div Am Soc Civ Eng* 96(4):835–855
14. Panizzo A, Girolamo PD, Risio MD, Maistri A, Petaccia A (2005) Great landslide events in Italian artificial reservoirs. *J Nat Hazards Earth Syst Sci* 5:733–740
15. Walder JS, Watts P, Sorensen OE, Janssen K (2003) Water waves generated by subaerial mass flows. *J Geophys Res [Solid Earth]* 108(5):2236–2255
16. Watts P (1998) Wave maker curves for tsunami generated by underwater landslide. *J Waterw Port Coast Ocean Eng* 123(3):127–137